Spectrally-selective solar absorbers based on Ta:SiO$_2$ cermets for next-generation concentrated solar-thermal applications

Maryna Bilokur, Angus Gentle, Matthew D. Arnold, Michael B. Cortie[*] and Geoffrey B. Smith

School of Mathematical and Physical Sciences, University of Technology Sydney, 15 Broadway, Ultimo, 2007, NSW, Australia

*Corresponding author.

E-mail address: Michael.cortie@uts.edu.au (Michael Cortie)

ABSTRACT

An iterative algorithm was used to design a spectrally-selective thin-film stack to provide maximum solar-to-thermal conversion efficiency at the very high operating temperatures associated with high solar concentrations. The resulting stack was then fabricated by magnetron sputtering and characterized. It was comprised of two Ta:SiO$_2$ layers with differing Ta nanoparticle content, on a refractory metal substrate. An SiO$_2$ anti-reflecting overlayer completed the stack. Optical and microstructural characterization indicated that the stack achieved 97.6 % solar absorptance up to 900 ℃. Spectral selectivity and thermal stability improved on annealing in two ways, first due to recrystallization of the Pt or Ta back-reflectors which lowered room temperature thermal emittance to 0.15 from 0.18, and to 0.14 from 0.21, respectively; and secondly due to alloying of substrate atoms with the Ta nanoparticles of the cermet.

Keywords: solar thermal conversion; spectrally-selective; solar absorptance; tantalum nanoparticles; thermal stability

1

1. Introduction

Conversion of solar energy to other forms of energy can be achieved with concentrator-based solar thermal technologies. A key requirement for efficient photo-thermal conversion in such devices is that their working surfaces must exhibit spectrally-selective solar absorption: high absorption at visible wavelengths combined with high reflectance at infra-red wavelengths. Furthermore, the spectrally-selective coating (SSC) must be able to withstand the elevated operating temperature which may reach 490 – 565 ºC in the case of parabolic trough power plants.[1] Extending this temperature to 630 ºC will result in the maximum power output of a concentrated solar power (CSP) plant, as was shown in ref.[2] These are key areas in which a new generation of advanced materials can play an important role.

A shift to even higher operating temperatures opens up possibilities for a new generation of emerging solar thermal technologies including thermionics and solar thermo-photovoltaics (STPV), **Figure 1**. In the latter, high enough temperatures from concentrated solar heating can in principle create thermal radiant photons spectrally suited to high conversion efficiency by a photovoltaic (PV) cell. It has been shown, for example, that raising operating temperature from 730 ºC to 930 ºC in some STPV systems results in an efficiency enhancement of more than 8 %.[3] It is challenging, however, to find suitable SSCs for STPV systems because, for the commonly used Ge PV cell with a bandgap of 0.67 eV, the generation of bandgap-matching photons requires absorber/emitter operating temperatures above 1300 ºC. This is in order to position the peak in the blackbody radiation spectrum at the desired energy. In contrast, STPV systems employing a InGaAsSb PV cell with a bandgap of 0.55 eV require lower energy thermal photons than Ge and, in this case, operation at 1007 ºC matches the emission peak to the bandgap.[4]
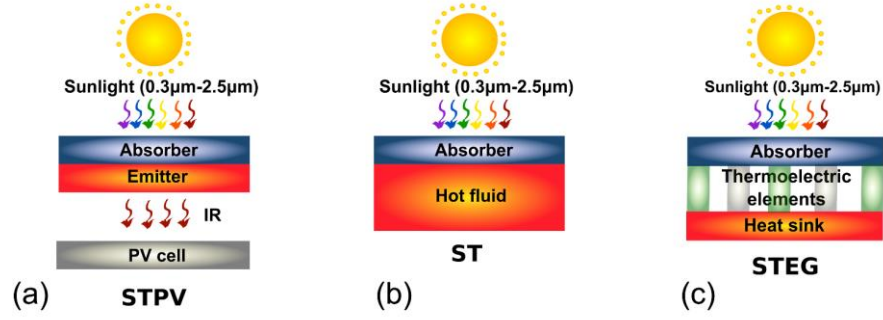
Figure 1. Harnessing of solar energy through solar thermal conversion through a) solar thermo-photovoltaics, b) solar thermal and c) solar thermoelectric generation.

Current designs of coating that provide a spectrally-selective response include multilayers, cermets, semiconductor-metal tandems, photonic crystal structures, and hybrid combinations of these structures. The double cermet stack pioneered by Zhang and Mills in 1992[5] is, however, a common choice. No matter which design is chosen, achieving both spectral-selectivity and structural thermal stability in the 630 ºC to 1000 ºC range is a challenge because different materials may exist in close proximity – for example a metallic infrared (IR) reflector, a cermet layer which includes a metal and a dielectric, and a dielectric anti-reflection (AR) layer may be juxtapositioned, and each of these has different thermal expansion coefficients and chemical reactivity. These factors cause generation of thermal stresses and possible degradation in service.

The ability of these coatings to absorb sunlight may be parameterized as solar absorptance, α_s:

$$\alpha_S = \frac{\int_{0.3\,\mu m}^{2.5\,\mu m}(1-R(\lambda))S(\lambda)\mathrm{d}\lambda}{\int_{0.3\,\mu m}^{2.5\,\mu m}S(\lambda)\mathrm{d}\lambda} \tag{1}$$

where spectral reflectance $R(\lambda)$ is measured at ambient and $S(\lambda)$ is the ASTM AM 1.5D solar spectrum. The term $\int_{0.3\,\mu m}^{2.5\,\mu m}S(\lambda)\mathrm{d}\lambda$ is, for all practical purposes, the solar flux, Φ. α_s ranges between 0 for a perfect mirror to 1 for a perfect absorber. Maximum conversion efficiency of the device also requires, however, that re-emission of the absorbed energy by conduction,

3

convection or re-radiation is minimized. Taking this into account, the net power out per unit area of a solar collector is[6]

$$P_{out} = X.\Phi.\alpha_s - \left[\epsilon_h.\sigma\left(T^4 - T_0^4\right) + L_{c,c}\right] \tag{2}$$

where X is the ratio of the collector area to the absorber area, ϵ_h is the integrated hemispherical emittance, σ the Stefan-Boltzmann constant, T the temperature of the surface of the coating, T_0 the temperature of the surrounding environment, and $L_{c,c}$ the power per unit area lost by conduction or convection. The heat extraction efficiency of the device is then[6]

$$\eta_{therm} = \frac{P_{out}}{X.\Phi} = \alpha_s - \frac{E\sigma\left(T^4 - T_0^4\right) + L_{c,c}}{X.\Phi} \tag{3}$$

η_{therm} may be maximized by a variety of strategies. While it is immediately obvious that ϵ_h and $L_{c,c}$ should be as small as possible, inspection of equation (2) also shows that it helps to concentrate the incoming radiation (increase X) while keeping the surface temperature of the device as low as possible. Unfortunately, if that same heat is to be converted to mechanical or electrical energy via a heat engine then the Carnot criterion,

$$\eta_{mech} = 1 - \frac{T_0}{T} \tag{4}$$

applies as well, where η_{mech} is the efficiency of converting thermal energy to mechanical energy. This is maximized if T is as large as possible and T_0 is as small as possible. The total efficiency is therefore

$$\eta_{tot} = \eta_{thermal}.\eta_{mech} \tag{5}$$

Balancing these conflicting factors complicates the design process for solar thermal devices, and the actual configuration depends on the desired purpose of the installation.
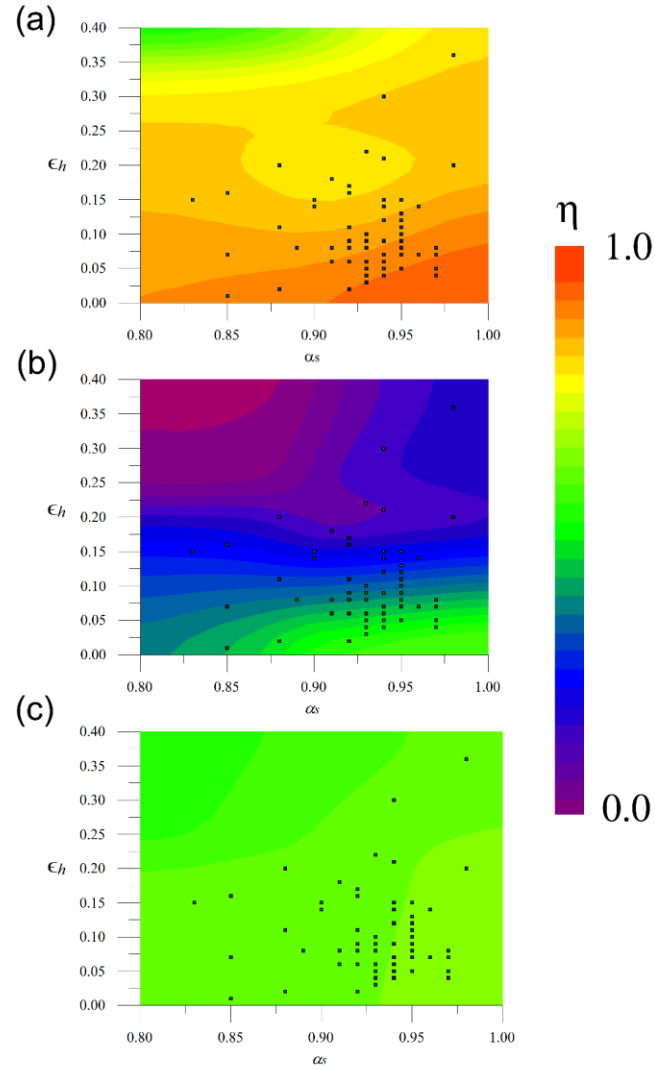
Figure 2. Efficiency as a function of α_s and ϵ_h, assuming $L_{c,c}$=0 and $T_{ambient}$ = 27 °C. Literature data for various coatings is over-plotted as black squares. (a) Case 1: $\eta_{thermal}$ for an installation designed to generate hot water at 100°C at a concentration of 1 sun (b) Case 2: η_{total} for an installation that will drive a heat engine at 600 °C to produce mechanical or electrical energy using a concentration factor of 9 suns. (b) Case 3: η_{total} for an installation that will drive a heat engine at 600 °C to produce mechanical or electrical energy using a concentration factor of 500 suns. The references from which these data points were collected are provided in the Supporting Information as Table S1.

It is useful to compare the optical properties of various known coatings by plotting their α_s and ϵ_h values, as well as $\eta_{thermal}$ and η_{total}. In **Figure 2** we take T_0 as 27 °C, Φ as 750 W.m^{-2}

5

[7] and consider three illustrative scenarios: hot water production at 1 sun concentration, mechanical work at 600 °C and 9 suns concentration, and mechanical work at 600 °C and 500 suns concentration (such as might be used in a point focus collector). Note that we have used ϵ_h as provided by various authors for measurements between 80 and 500 °C. In general, the hemispherical emittance may depend on temperature, but here we use the values provided 'as is' in order to provide a broad-brush summary of the situation.

It is clear that an efficiency of ~0.9 for generating water at 100°C is quite readily attainable with current coatings. (Of course, the total power drawn would have to be limited to maintain the water temperature at 100°C.) Adequate production of mechanical energy at 600 °C and 9 suns on the other hand is only feasible with the very best coatings and even then η_{total} will only be ~0.5. Increasing the flux to 500 suns does not increase the maximum efficiency possible (which is limited by the Carnot efficiency in this scenario), but it does allow the window of suitable optical properties to be opened up considerably, to the extent that any (stable) coating with $\alpha_s > 0.8$ and $\epsilon_h < 0.4$ will provide adequate performance.

In the present work, a significant improvement in spectrally-selective response is demonstrated. This result is particularly helpful for a scenario like that of Figure 2b, in which solar energy is converted to mechanical work and hence electrical energy at a solar concentration $1 < X < 10$. While the primary goal was to design a SSC for high temperature operation of parabolic trough solar power plants in the aforementioned envelope, the SSC was also tested in the 700 °C to 1000 °C range in order to investigate its potential exploitation for STPV devices. We show that a superior solar absorptance of nearly 98% can be achieved for a Ta:SiO₂ stack consisting of two cermet layers with differing Ta content. The stack also showed a low thermal emittance. Furthermore, the stack survived heat treatments up to at least 900°C under vacuum, which, to our knowledge, has not been achieved yet for a cermet-based solar absorber. This coating on refractory metal is exceptional in its combination of nearly ideal spectral selectivity and retention of optical properties to very high temperatures.

2. Results and discussion

2.1 Structural characterization of Ta:SiO$_2$ stacks

Two types of SSCs were developed in this work, **Figure 3**a and b. The two stacks included four principal layers: IR reflector (Pt or Ta), high metal volume fraction (HMVF) cermet layer (Ta:SiO$_2$), low metal volume fraction (LMVF) cermet layer (Ta:SiO$_2$), and AR layer (SiO$_2$). The cermet consisted of nanoparticles of Ta metal within a SiO$_2$ matrix. Tantalum is very refractory both on its own and when it forms compounds with boron, nitrogen, carbon, and alloys or intermetallic with selected metals. It is also used as a replacement for platinum in laboratory equipment that must be highly corrosion resistant. The potential of Ta for high temperature CSP applications has been investigated by other workers as a photonic crystal structure,[8] as tantalum thin films,[9] and as a diffusion barrier in spectrally-selective multilayer structures.[10] However, to our knowledge, Ta was never investigated previously for use as the metallic nanoparticle in a cermet-based SSC. In the present work a SiO$_2$ host matrix was chosen due to its proven thermal stability when used as a host matrix in other SSC metal-insulator composites.[11] Pt or Ta were chosen as back-reflectors as they have a high oxidation resistance and reasonably high (about 820 and 1400°C respectively) eutectic points with Si. Other refractory metals, such as W, Ni or V are less oxidation resistant. The volume of the Ta particles within the two cermet layers was optimized to achieve the highest possible solar absorptance α using the theoretical model developed in the WVASE software with the Bruggemann EMA approximation.[12] Results are shown in Figure 3d. As seen in Figure 3d, the optimal Ta content for the HMVF layer is in the 38 - 50 vol% range, and for the LMVF on top is in the range 16 - 26 vol% of Ta. The best theoretical iteratively refined values for the combination of both layers were 42 vol% and 20 vol% respectively. With these, a maximum α_s surpassing 97% was predicted. The good agreement of the simulation to the measured reflectance spectrum of the stack is clear in Figure 3e. This plot shows that the design produced by the iteration strategy is actually achievable in practice using a sputtering deposition system.
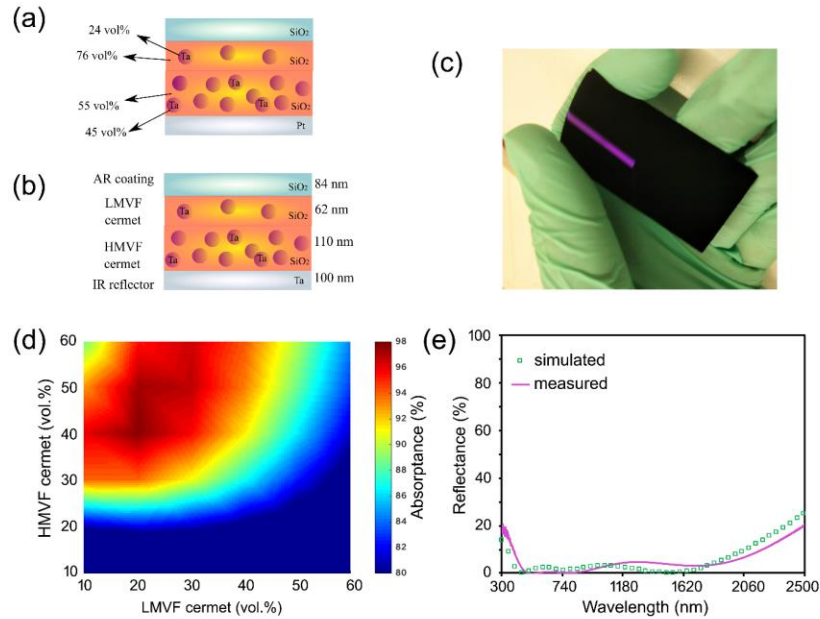
7

Figure 3. Design of the sputtered Ta:SiO$_2$ cermet based SSCs. a) Ta:SiO$_2$ stack using Pt reflector, b) Ta:SiO$_2$ stack using Ta reflector, c) top view of stack on Ta substrate, d) Effect of a metal fraction in the cermet layers on optical response of the Ta:SiO$_2$ stack, e) comparison of the theoretical and measured optical response of the optimal Ta:SiO$_2$ stack using Pt as a back-reflector.

The SEM cross-sectional images in **Figure 4** show the evolution of the microstructure in this stack. Sharp boundaries are apparent between each layer. The variation in image contrast between the layers indicates that metal is present, with indications of relative metal content and its crystallinity within metal-containing layers. The outer Ta:SiO$_2$ layer with 24 vol% of Ta shows darker interface contrast compared to that with 45 vol% of Ta. Annealing of the Ta:SiO$_2$ solar absorber at 600°C does not lead to any significant structural modifications and the initial boundary and contrast between the layers is preserved, indicating good dimensional thermal stability of the cermet layers. This dimensional stability continues with further annealing steps at 700 °C, 800 °C and 1000 °C, but annealing at 700 °C led to obvious recrystallization of the Pt back-reflector from its initial dense columnar structure. This metallization will be shown later to result in emittance reduction. Finally, spherical metallic nanoparticles can be discerned in the top cermet layer after annealing at 900 and 1000 °C, a feature that is absent from the samples subjected to lower temperature

processing. It is important to note that the layered structure of the coating was preserved during annealing even though chemical reactions occurred between the coating constituents. Finally, the observed shape acquired by the metallic inclusions is in agreement with the changes that occur in ellipsometrically-derived effective medium models, which we will now discuss.
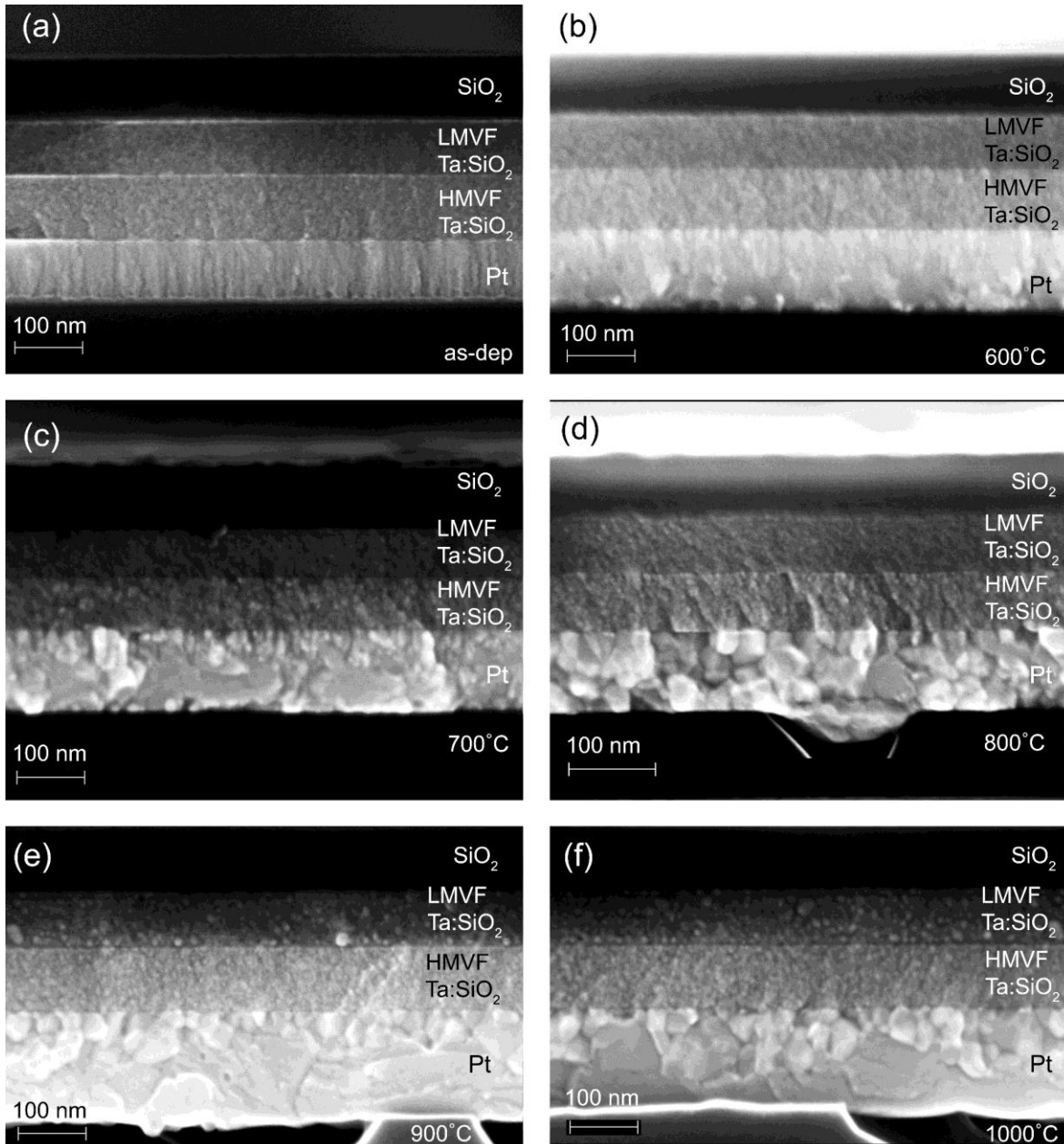

Figure 4. Cross-sectional SEM images of Ta:SiO₂ stack using Pt back-reflector, a) as-deposited, b) annealed at 600 °C , c) 700°C, d) , 800°C, e) 900°C, f) 1000°C

2.2. Ellipsometric characterization of individual Ta:SiO₂ cermet layers

The fitting of the optical constants was conducted by building a general oscillator model. Depending on whether the material type is a metal, semiconductor or insulator, a different set of oscillators was used in particular spectral ranges. In addition some will spectrally overlap, for example, inter-band and "free" carrier responses partially overlap in bulk Ta.[13] For the deposited Ta:SiO₂ cermet layers, Lorentz, Tauc-Lorentz and Drude oscillators were all needed. The contribution of polarized bound electrons in the UV and visible range required Lorentz and Tauc-Lorentz oscillators, while conducting charge carriers needed a Drude oscillator at longer wavelengths. When the Drude response stands alone, its complex dielectric constant ($\tilde{\varepsilon}$) can be defined as:[14]

$$\varepsilon = \varepsilon_1 + i\varepsilon_2 = \varepsilon_\infty - \frac{\omega_p^2}{\omega^2 + i\omega\omega_\tau} \tag{6}$$

where ε_1 and ε_2 are the real and imaginary parts of $\tilde{\varepsilon}$ respectively; ω_p is the bulk plasma frequency while the shielded plasma frequency $\omega_P^* = \omega_p/\varepsilon_\infty^{1/2}$ is where ε_1 becomes negative; ω_τ is a the angular frequency of carrier loss rate and ω the angular frequency of the radiation.

The optical constants *n, k* of the two Ta:SiO₂ cermet layers were derived from the psi and delta spectral parameters established from ellipsometry, **Figure 5**. They were modeled using the two topologically distinct effective medium approaches to nanoparticle doping, which depend on whether the Ta doping density was high or low. In the former, percolation with associated Drude response occurs, so the Bruggeman[12] Effective Medium Model (EMA) gave the best fit, as expected. The appropriate best fit EMA model for lower doping was instead found to be that of Maxwell-Garnett.[12, 15] Therefore, we used a MG medium layer sitting above a percolating network layer. The resulting *n, k* plots for both samples are depicted in Figure 5c after best fit of the volume fraction of metal was found. The two concentrations of Ta nanoparticles needed were 24 vol% and 45 vol% to match the data in Figure 5.

10

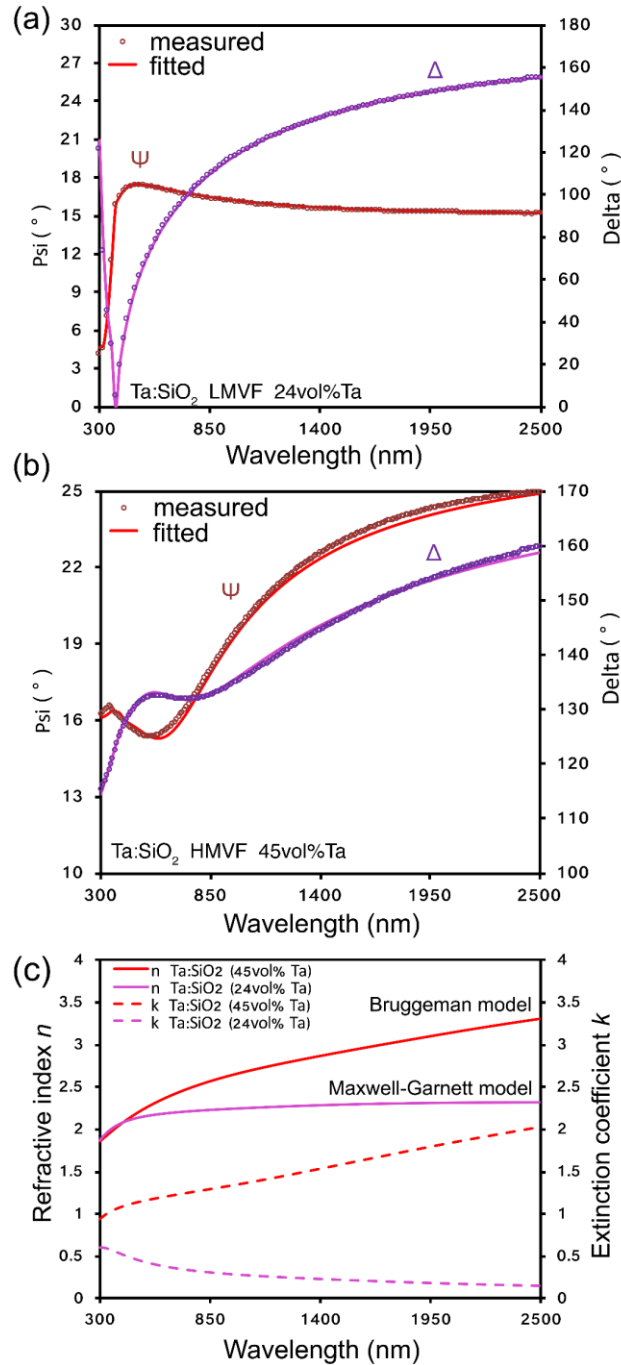**Figure 5.** Measured psi and delta parameters for the LMVF and HMVF Ta:SiO$_2$ single layers and the ellipsometric fit using oscillator-based effective medium models. The psi plots are quite different due to percolating topologies (a) and isolated particles (b). (c) The optical constants of the two Ta:SiO$_2$ cermet layers with low and medium Ta nanoparticle content, showing localized and percolating responses respectively.

The Bruggeman EMA approximation is preferable for two-phase media when the volume fraction of metal inclusions is high enough for some percolation. For optical fields (but not for dc fields) this commonly occurs in the 30 to 40 vol% range. Optical frequency partial percolation can thus set in at much lower concentrations than in dc measurement as optically percolating clusters can be much shorter than the span between typical dc electrodes.[12, 15] For the current cermet with 45 vol% of Ta, n, k increase steadily with wavelength, which is typical of percolating metal. We can show that most Ta in the 45% composite is in percolating networks as follows: if it was, we would expect ω_P to vary as $(f)^{1/2}$ with f metal volume fraction and all carriers present contributing. Thus, if we have the correct f value from ellipsometry, we might expect $\omega_P(\text{cermet}) = 0.45^{1/2} \, \omega_P(\text{bulk Ta}) = 5.9$ eV as $\omega_P(\text{bulk Ta}) = 8.8$ eV. The 5.9 eV result is close to the Drude fit of 6.3 eV. The reverse calculation of f from experimental $\omega_P(\text{cermet}) = 6.3$ eV gave $f=0.51$ compared to the EMA fit of 0.45. For the LMVF Ta:SiO$_2$ layer, a Maxwell-Garnett EMA gave an exact fit to psi and del. For the composite with $f = 0.24$ for Ta in SiO$_2$, this concurs with the low filling factor f of the Ta inclusions as most particles will be isolated or in small enough clusters not to optically percolate. The optical constants of this low f layer are typical of a semi-metal, where the extinction coefficient monotonically falls as wavelength lengthens. These two layers with a low refractive index top layer such as SiO$_2$ enables better impedance matching to the exterior by the solar absorber. Enhanced solar absorption within the graded stack results.

The effective carrier damping frequency $\omega\tau$ in the percolating network was fitted as 5.9 eV, about nine times higher than that of bulk Ta of 0.67 eV.[13] This increase might in part be the result of a very high rate of collision of carriers with metal surfaces or internal defects in percolating but bending Ta filaments. It may also indicate a misleading fit of oscillator broadening due to the band overlap noted above. Optical data well beyond the solar spectral range, where small band gap effects are no longer present, would be needed to separate the two possible, partially overlapping broadening effects. It appears to be a common problem in a number of compound and refractory metal conductors where inter-band or defect absorption is present from the NIR out to a few μm (or to below 1 eV).

2.3 Ellipsometric characterization of multilayer stacks

The Ta:SiO$_2$ cermet-based multilayer solar absorbers employing the structural elements shown in Figure 3a and 2b, were characterized with ellipsometry before and after each annealing step. The measured and fitted psi and delta parameters are provided in the Supporting Information as Figures S1 and S2. For a best fit, a four-layer model was built using WVASE software, consisting of the Si substrate, Pt or Ta IR reflecting base layer, the two cermet layers with different Ta fractions, and an outer layer of SiO$_2$. The EMA approximations described in the previous section were used to fit the composition of both cermet layers within the stack, while the Pt, Ta and SiO$_2$ layers deposited were characterized in advance. These *n*, *k* values were then used in starting models for each layer present. In doing so, the starting point for final fits was based on component layers within the stack being produced with the same deposition conditions as used for the single layers that had already been characterized. This included the use of *n, k* from our Ta IR reflector films as the starting *n, k* for the Ta nanoparticles. The first additional parameter set was the volume fraction of the Ta in the LMVF layer, the second that in the HMVF layer, the third parameter fitted was the depolarization factor (DF) of the Ta particles, to account for a change in the shape during heat treatment. In our opinion, the fitting process was robust and physically meaningful because (i) only minor changes from the starting values were needed to achieve convergence, (ii) the resulting models were consistent with SEM observations of thickness and of particle shape, (iii) the models matched the predictions of the initial optimized stack designs and, finally, (iv) the models produced a realistic evolution of responses after 1 hour thermal treatment in vacuum at 600ºC, 700ºC, 800ºC, 900ºC, 1000ºC for the layers within each stack.

The model for the Ta:SiO$_2$ stack built on a Pt IR reflector is discussed first, then that for the stack built on the Ta reflector.

2.3.1 Pt back-reflector

The as-deposited Ta:SiO$_2$ solar absorber on Pt gave a close fit to optical data using $f = 0.24$ for Ta in the LMVF layer and $f = 0.45$ for Ta in the HMVF cermet plus a depolarization factor (DF) of 0.183 for the fit parameters of Figure S1. This DF value suggests an oblate shape of the un-annealed metal particles as also found in[15] and [16] (in comparison, a sphere should have a depolarization factor of 0.333). Annealing at 600 ℃ in vacuum did not lead to noticeable changes in the top cermet layer or in the shape of its Ta particles, indicating a high level of thermal stability for the top cermet layer. However, there were some changes in the cermet layer adjacent to the Pt reflector. In this layer, thermal treatment induced diffusion of some Pt into the cermet to about 0.3 vol%, in agreement with the XRD results (not shown here) which indicated that conversion of the Ta to intermetallic compounds had taken place. As shown in the spectroscopic characterization section, this change is beneficial as it causes a gain in the integrated solar absorptance of the whole stack. Further annealing at 700 ℃ and 800 ℃ led to gradual reshaping of the Ta particles in the top cermet. They acquired a more spherical shape relative to that of the initial Ta particles with depolarization factors of 0.20 and 0.23 respectively. The content of Ta inclusions remained unchanged, at around $f = 0.24$, demonstrating the absence of Ta metal particle diffusion from the bottom cermet layer into the top cermet at 600 °C.

The 700 ℃ and 800 ℃ thermal treatments did facilitate, by diffusion from the substrate, an overall increase of the Pt vol% in the bottom cermet layer to 1.5 and 3.5 vol%, respectively. These changes also had a beneficial effect on the solar absorptance. Annealing at 900 ℃ caused the quantity of Pt present in the bottom cermet to increase to 6 vol% (Supporting Information, Figure S1e). The 1000 ℃ heat treatment caused further minor reshaping of the Ta particles in the upper layer to DF = 0.26 compared to their initial 0.183 while the Pt content was increased to about 10% (Figure S1f) compared to the as-deposited value. These changes did not affect the absorption capabilities of the multilayer stack to any significant degree as the α value of the Ta:SiO$_2$ stack remained within the 94 - 96% range.

2.3.2 Ta back-reflector

The ellipsometric characterization of the annealed Ta:SiO$_2$ SSC is shown in the Supporting Information as Figure S2. In the fitting process, minimum Ta volume fractions of f=0.46 and f=0.24 were set in the HMVF and LMVF at respectively, and then additional metallic material allowed to accrue in order to fit the experimental data. The additional fraction of metal required rose steadily from $\Delta f = 0$ to 0.0028, to 0.0067, to 0.028 then 0.054 as the annealing temperatures were raised from 600 to 1000 °C. A corresponding gradual evolution of the depolarization factor of the LMVF towards a more spherical metallic particle (DF=0.17 to DF=0.21) demonstrates a similar trend to that of the stack deposited on the Pt back-reflector.

2.4. Spectroscopic characterization and emittance measurement

The spectrally-selective response of the Ta:SiO$_2$ multilayer stack with Pt reflector was analyzed by combining the measured spectroscopic data in the UV-vis-near IR range with that in the mid- and far-IR range, **Figure 6**. Also shown on the diagram are the standard solar spectrum and curves corresponding to black body radiation at 500 °C and 630 °C. This stack demonstrates a broad solar absorptance from 300 nm up to 2500 nm and high reflectance in the infrared. The calculated α shows that this two-layer cermet is capable of absorbing a remarkable 97.5% of incident solar radiation, with nearly 100% absorptance occurring between 470 nm and 620 nm. This represents one of the highest solar absorptance values achieved to date for cermet-based spectrally-selective solar absorbers that are also able to endure high temperature exposure up to 1000 ºC. The results can also be compared to a similar plot in our previous work on a Ti$_{1-x}$Al$_x$N stack where the coating exhibited an α value of 92.0%.[17] The improvement in the present coating is essentially due to the steeper transition between absorption and reflection at about 3300 nm. Prior Pt:Al$_2$O$_3$[18] and Cr:Al$_2$O$_3$[19] cermet-based solar absorbers have also demonstrated solar absorptance of 98%, however these stacks suffered degradation of α after annealing at much lower temperatures than used in the present work. The present Ta:SiO$_2$ double cermet solar absorber not only gave an initial very high level of solar absorptance, but preserved it throughout sequential step-ups in annealing temperatures to 1000 ºC. The optical transition between high solar

absorptance and high IR reflectance occurs within the range 2500 nm - 4500 nm, which results in a high degree of spectrally-selective response of our stack. The best design had a transition centered at 2500 nm, which is ideal for CSP applications in the 500 ℃-600 ℃ range. If a hotter Ta:SiO$_2$ is to be used, for heat or power including solar thermo-photovoltaic applications, then the cut-off must be pushed towards shorter wavelengths due to the shift in the black body radiation spectra at temperatures above 600 °C. Models show this cut-off can be achieved by tuning the volume fraction of Ta in both cermet layers plus associated thickness adjustment of each.
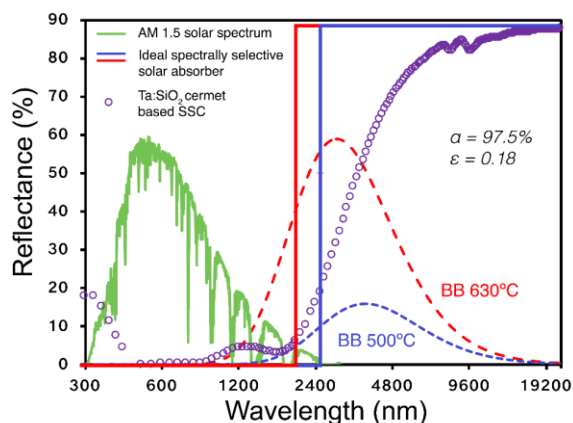

Figure 6. Measured spectrally selective response of the Ta:SiO$_2$ stack on Pt with a comparison to shifted ideal spectrally selective transition points at operating temperatures of 630 °C and 500 °C with the corresponding black body reference spectra.

The as-deposited measured thermal emittance was 0.18 with the Pt substrate and 0.21 for that with the Ta substrate. Operating at higher temperatures causes a shift in the Plank spectrum towards the solar wavelength range with a consequent changes to emittance (Supporting Information, Table S2). The coatings are spectrally-selective to absorb strongly in the solar range so as to maximize absorbed solar energy but, as the surfaces experience increasingly higher temperatures, they begin to emit at the shorter wavelengths causing an overlap between the thermal emission and the desired absorption of solar energy, leading to a higher emittance. Therefore a fine balance between the cut-off wavelength for strong

16

absorption, concentration factor of the solar energy, and operating temperature must be considered.

Figure 7a and b shows the combined spectral and angular dependent reflectance of the designed $Ta:SiO_2$ cermet stack on Pt. The angle of incidence dependence of α_s is a key characteristic used in single axis tracking[12] but is rarely studied. These measurements show that the $Ta:SiO_2$ stack is an excellent absorber over a broad angular range with α of 97.5% out to 40º incidence and 96.2% to 50º and spectral response remains very high from 350 nm to 2000 nm. α_s declines to a still useful 85% at 70º and 65% at 80°. These results are comparable to that of the $Ni:Al_2O_3$ solar absorber developed by Tesfamichael, which exhibited 95% solar absorptance at 50º and 80% at 70º,[20] and for the $Mo:SiO_2$ cermet developed by Zhang.[5] Our angular dependence of α for this $Ta:SiO_2$ cermet absorber is in agreement with Fresnel equation models of reflectance for this stack as the incidence angle increases.
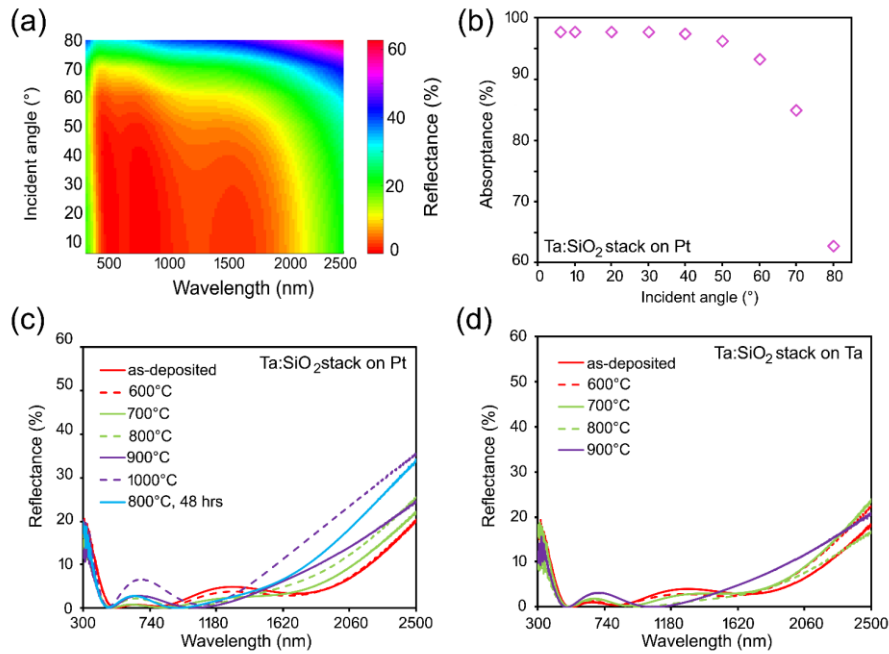

Figure 7 a) Measured reflectance of the $Ta:SiO_2$ stack on Pt reflector as function of the incident angle of the light, b) calculated integrated solar absorptance, (c) reflectance spectra of $Ta:SiO_2$ stacks on Pt back-reflector as-deposited and after each annealing heat treatment, (d) as for previous panel but for $Ta:SiO_2$ stack on Ta back-reflector.

The measured reflectance of Ta:SiO$_2$ cermet-based stacks on Pt and Ta before and after annealing are shown in Figure 7c and 7d. Both stacks show nearly identical reflectance patterns before annealing with a broad absorptance across the solar spectrum and two characteristic interference humps resulting from reflections at the boundaries of the four different layers with their particular *n* and *k*. The calculated solar absorptance values are 97.5 % for the Ta:SiO$_2$ stack on Pt and 97.6 % for the Ta:SiO$_2$ stack on Ta. An initial annealing in vacuum at 600 ℃ did not lead to any significant optical response changes in either stack with a minor reduction of the broad interference hump located around 1200 nm causing a slight increase in solar absorptance of 0.2 %. As discussed above, this is due to a slight increase in the metal particle fraction within the HMVF layer caused by thermally-activated diffusion of the metallic atoms from the back-reflectors. The change further flattens the internal interface-based interference shoulder and brings the solar absorptance of the Ta:SiO$_2$ stack on Pt to 98.2 %. A slight increase after annealing in the reflectance in the near-IR range is attributed to two phenomena: firstly, an increase in the metallic fraction in the HMVF layer, as discussed above, which enhances percolation within the cermet layer for a higher reflectance in the NIR range, as seen in Figures S1 and S2, secondly the emittance measurements show a reduction in the thermal ϵ_h value for both stacks, from 0.18 to 0.15 (on Pt) and from 0.21 to 0.14 (on Ta), Table 1. This is likely be due to grain growth within the back-reflector layers which enhances their IR reflectance.

Annealing at 800℃ leads to a further changes from those to 700°C of *n, k* in the HMVF cermet layer which resulted in flattening of the interference hump near 700 nm. This heat treatment led to the highest value of solar absorptance achieved (98.4%) in this study, along with a low ϵ_h. This excellent result followed from the combination of a near-ideal amount of metal content in the HMVF cermet plus weakened interference effects between layers due to the intrinsic absorptance in the cermets, as predicted with optimized optical modeling of such stacks. Further annealing to 900 ℃ shows that both Ta:SiO$_2$ cermet-based stacks are stable in an optical sense, maintaining very high solar absorptance (97.4 %) and low thermal emittance. The stack on the Pt back-reflector was even able to resist annealing up to 1000 °C (Figure 3f).

18

Of course, thermal emittance at actual operating temperatures will differ from the room temperature values. Up to five physical factors can alter sample ϵ_h values at successively higher operating temperatures: (i) the blue shift of the black body spectrum, (ii) increased carrier collision rates within hotter metals, (iii) decreased carrier collision rates (from grain boundaries) as grain size grows, (iv) decreased grain boundary loss if grains are better able to align, and (v) addition of nano-scale roughness on an interface causing plasmonic resonant loss. Given the stability observed in morphology and the grain growth effects shown above, a large rise in ϵ_h is not expected in the present case. In addition, as shown in Figure 2, higher operating temperature requires much larger concentration factors C so a lower ϵ_h value has decreasing impact on output loss when operating at above 700 °C, though it is still quite important for operation at 600 °C as indicated above.

Table 1. Solar absorptance and hemispherical thermal emittance (both measured at room temperature) versus annealing temperature. Solar absorptance values have been rounded to one decimal place, thermal emittance to two decimal places.

Temperature, °C	Ta back-reflector		Pt back-reflector	
	α	ϵ_h	α	ϵ_h
As-deposited	97.6	0.21	97.5	0.18
500	97.8	0.18	97.7	0.18
600	97.7	0.15	98.2	0.17
700	98.4	0.11	97.7	0.16
800	97.4	0.14	97.5	0.15
900	-	-	94.9	0.15

An excellent spectrally-selective response is thus maintained at the higher temperatures. This impressive result suggests that a Ta:SiO$_2$ solar absorber stack can potentially be operated in the 600 to 800 ºC range in CSP applications without sacrificing solar absorptance or significant spectral-selectivity. Negligible degradation occurred after 10 hours at 800 ºC in vacuum, which implies applications in parabolic troughs should maintain long term spectral- selectivity. The final long-term stability test showed that the Ta:SiO$_2$

stack on the Pt reflector survived 800 ℃ continuous annealing for 48 hours for a stable solar absorptance of 97% and preservation of spectral-selectivity, with low ϵ_h of 0.15. As expected, a rise in the reflectance occurs in the mid-IR due to increased optical percolation within the dielectric matrix caused by an increase in the metallic volume fraction. Simultaneously, a changed conductivity in the Pt IR back reflector caused by its recrystallization and reaction with silicon is also likely to modify NIR response. Overall, these changes both contribute positively to the spectral-selective solar performance of the Ta:SiO$_2$ stack.

3. Conclusion

Ta:SiO$_2$ double cermet spectrally-selective solar absorbers deposited on Pt and Ta back-reflectors were designed using an iterative algorithm, fabricated, and then tested. A remarkably high value of solar absorptance (97.6 %) with a low thermal emittance (0.21) resulted by first optimizing modeled optical responses of the double layer cermet by varying the Ta nanoparticle fractions within each cermet layer, along with tuning the thickness of the outer anti-reflective layer. The optimized stack was then fabricated with controlled co-sputtering. These solar absorbers were exposed to a series of thermal annealing tests up to 1000 ℃ in order to test the possibility of their long-term use in high temperature solar thermal power plants, and their potential for emerging applications requiring operating temperatures higher than 700 °C. High temperature annealing of the coating deposited on the Pt back-reflector did not appear to change the top cermet layer significantly, but did cause an increase in volume fraction of the metallic phase in the inner layer. This was evidently due to Pt and Si diffusing upwards from the back-reflector layer and alloying/reacting with the Ta particles of the cermet. The Pt-based stack achieved 98.4 % solar absorptance upon being exposed for an extended time at 700 °C. In the case of the coating on the Ta back-reflector, the main alterations were a change in shape and volume fraction of the Ta particles. In both cases these changes had a beneficial effect on solar absorptance.

4. Material and methods

   Experimental: Two types of spectrally-selective solar absorbing coatings were initially deposited on Si substrates using a DC magnetron sputtering system without heating. The main difference between them was that they had different metal substrates for IR reflection. Prior to the deposition process, the vacuum chamber was evacuated to a base pressure of 3.7×10^{-4} Pa (2.8×10^{-6} Torr). The Si substrates were ultrasonically cleaned in an acetone and ethanol bath for 80 minutes in total. High purity targets Ta (99.99%), Pt (99.99%) and SiO_2 (99.99%) with a diameter of 50 mm were used. The targets were cleaned for 1 minute in Ar-plasma prior to the deposition.

   An IR reflector of either Ta or Pt was the first layer deposited on Si. These Ta or Pt metal films were deposited at Ar pressure of 0.21 Pa and 0.17 Pa (1.6 mTorr and 1.3 mTorr) respectively, with a target current of 0.15 A for both metals.

   For the cermet layers, co-sputtering of the Ta target and the SiO_2 target was performed. Ar was introduced to the chamber at the pressure of 0.19 Pa (1.4 mTorr) for deposition of two $Ta:SiO_2$ layers, first one with high metal volume fraction (HMVF) and then one with low metal volume fraction (LMVF). Finally, an anti-reflective (AR) SiO_2 layer was added with the chamber pressure at 0.17 Pa (1.3 mTorr). The Ta filling factor in the cermet was controlled by varying the input power applied separately to the targets at 0.04 A for the LMVF and at 0.09 A, for the HMVF. An RF power supply was used at 132 W in depositing both cermet layers and the AR SiO_2 layer. The thickness of the thin films was monitored using a quartz crystal monitor installed inside the deposition chamber.

   To test the potential of the cermet-based SSCs for high temperature CSP applications, the multilayer composites were first exposed to 600°C in a vacuum tube furnace pumped down to 1.3×10^{-3} Pa (10^{-5} Torr) for 30 minutes and then to 1 hour at 700 °C, 800 °C, 900 °C, 1000 °C and 1100 °C using a Denton thermal evaporation chamber pumped down to 1.3×10^{-3} Pa, where the samples were taken out of the furnace for *ex situ* characterization between each heat treatment. To identify the microstructural features of the coatings, images of cross-sections were taken with a ZEISS EVO scanning electron microscope at 20 kV.

   The spectral reflectance was obtained using an Agilent Cary 7000 Universal Measurement Spectrophotometer (UMS) covering the 300-2500 nm wavelength range (angle of incidence 8°). The absorptance spectrum $A(\lambda)$ was obtained according to the formula $A(\lambda)=1-R(\lambda)$ using measured

reflectance $R(\lambda)$. $T(\lambda)$ is assumed to be zero for the two types of absorbers on opaque IR metal reflectors. The emittance of solar absorbing coatings for solar thermal applications was measured using a Perkin Elmer 100 FTIR at room temperature. In all cases the spectral property can be taken as being at normal incidence. Performance at elevated temperatures was estimated using the black body spectrum at the relevant temperatures and the room temperature reflectance. Spectroscopic ellipsometry using a J.A. Woollam Co., Variable Angle Spectroscopic Ellipsometer (VASE) was used for determination of the optical constants over the solar range (300 to 3000 nm), with measurements taken in 5 nm steps at angles of 60°, 70° and 75°.

For a comprehensive analysis of these spectrally-selective solar absorbers, a theoretical model of the stack was built using the WVASE software (J.A. Woollam Co.). The generated results were obtained by fitting to the experimentally measured ellipsometric parameters and measured reflectance spectra, and then were displayed in terms of the final reflectance spectra for the best fit multi-layer model of the coating.

Design of stack: A nearly ideal solar absorptance by a cermet-based Ta:SiO_2 stack was systematically designed using an iterative procedure based on sequentially modifying stack compositions followed by construction of a multilayer model based on the available ellipsometry data. In this approach, the WVASE software was used to build a theoretical model which maximized both solar-selective optical response and α of the absorber/substrate combination, in an iterative fashion. The algorithm used is shown in a flow chart (Figure S3, Supporting Information). The iteration used took seven cycles and after each cycle one key additional basis for the ideal spectrally-selective absorber was set. The first cycle was comprised of the selection of the IR back-reflector. This step enhanced performance by preventing heat loss by radiation. A high spectral-selectivity ratio $\alpha \, \epsilon_h$ is of significant value for most efficient heat production at up to about 700 °C. Maximizing α by itself becomes the major consideration at higher temperatures such as would occur in devices with higher concentration factors. Maintaining a low ϵ_h at the higher temperatures can still add value to conversion though, as well as being an indicator of good thermal stability. The second part was made up of a more complex procedure, where optical compatibility of the metal particles and dielectric matrix was assessed to create a cermet layer with optimal thickness and volume fraction of metal particles within the host. If a nearly ideal solar absorber was achieved at

22

this stage, then the optical model was transferred to the experimental stage for testing. Of course, an exact reproduction of the theoretical design is not possible due to the practical limits of the deposition process, in particular it was not possible to control thickness to an accuracy of better than about ± 2 nm, or composition to better than about ± 1%. Residual contaminants may also become attached on the surface. Such deviations can modify the position and amplitude of the peaks in the measured reflectance/absorptance spectrum, leading to reduced α/ϵ_h and α. The level of crystallinity and grain boundary scattering is also influenced by deposition conditions. For example, carrier loss rate in metals is influenced by the microstructure and this can modify the refractive index of the back-reflector and cermet layers.

Further improvement in efficiency with added cycles can be achieved if α is not high enough. In particular it was found useful to add an additional cermet layer with a modified metallic particle volume fraction. The composition in the original and the new cermet layer must both be adjusted for best response. A graded Ta volume fraction would be the limiting situation but is not actually needed to achieve a very high α and would be harder to accurately reproduce during deposition. In addition, the incorporation of an AR layer on a two-layer cermet stack turns out to be just as beneficial. This also serves as a dense layer protection against oxidation or deterioration of the lower layers. A final improvement after selection of the main absorbing layers and a basic dense AR layer is to see if additional broadband impedance matching to the incoming solar radiation is possible. This last improvement can push α very close to 100 % and is introduced within the theoretical models using either roughening or pores in the outer dielectric layer. Samples with such outer layers may however be more prone to chemical or mechanical damage at elevated temperature.

Fewer layers in the stack are generally preferable for stability during annealing, particularly due to generation of less thermal stress as a result of thermal expansion coefficient mismatch between adjacent materials. Constructing an optimized cermet-based SSC for high temperature CSP applications thus involves balancing three key aims: (i) very high solar absorptance, (ii) low thermal emittance, and (iii) long term thermal stability of α and ϵ_h. Changes in emittance ϵ_h occur with or without changes in morphology or chemistry. As noted above, achieving a higher operating temperature with a rise in concentration factor X means a moderate rise in ϵ_h can be tolerated above 700 °C.

In the current study four iteration cycles were used to reach the desired spectrally-selective response based on a double cermet Ta:SiO$_2$ absorber alone. The optimization iteration cycle was concluded at a 97.5 % solar absorptance. A further boost to 99 % was found from our models when impedance matching to the incoming radiation (using the low index layers noted above) was added.

Supporting Information

Supporting Information is available from the Wiley Online Library or from the author.

Acknowledgements

References

[1]   M. Romero, A. Steinfeld, *Energy & Environmental Science* **2012**, *5*, 9234.
[2]   W. Y. Lee, S. S. Kim, *International Journal of Energy Research* **1991**, *15*, 257.
[3]   P. Bermel, M. Ghebrebrhan, W. Chan, Y. X. Yeng, M. Araghchini, R. Hamam, C. H. Marton, K. F. Jensen, M. Soljačić, J. D. Joannopoulos, *Optics Express* **2010**, *18*, A314.
[4]   V. Rinnerbauer, A. Lenert, D. M. Bierman, Y. X. Yeng, W. R. Chan, R. D. Geil, J. J. Senkevich, J. D. Joannopoulos, E. N. Wang, M. Soljačić, *Adv. Energy Mater.* **2014**, *4*, 1400334; A. Lenert, D. M. Bierman, Y. Nam, W. R. Chan, I. Celanović, M. Soljačić, E. N. Wang, *Nat. Nanotech.* **2014**, *9*, 126.
[5]   Q. C. Zhang, D. R. Mills, *J. Appl. Phys.* **1992**, *72*, 3013.
[6]   R. E. Hahn, B. O. Seraphin, *Phys. Thin Films* **1978**, *10*, 1.
[7]   G159-98, American Society for Testing and Materials (ASTM), **1998**.
[8]   Y. Nam, Y. X. Yeng, A. Lenert, P. Bermel, I. Celanovic, M. Soljačić, E. N. Wang, *Solar Energy Mater. Solar Cells* **2014**, *122*, 287; V. Rinnerbauer, Y. X. Yeng, W. R. Chan, J. J. Senkevich, J. D. Joannopoulos, M. Soljačić, I. Celanovic, *Optics Express* **2013**, *21*, 11482.
[9]   V. Rinnerbauer, J. J. Senkevich, J. D. Joannopoulos, M. Soljačić, I. Celanovic, R. R. Harl, B. R. Rogers, *J. Vac. Sci. Technol. A: Vacuum, Surfaces, and Films* **2013**, *31*, 011501.
[10]   Z. Nuru, C. Arendse, S. Khamlich, L. Kotsedi, M. Maaza, *Solar Energy* **2014**, *107*, 89.
[11]   J. Wang, B. Wei, Q. Wei, D. Li, *physica status solidi (a)* **2011**, *208*, 664.
[12]   D. Bruggemann, *Ann. Phys* **1935**, *24*, 636.
[13]   P. Romaniello, P. de Boeij, F. Carbone, D. Van Der Marel, *Phys. Rev. B* **2006**, *73*, 075115.

[14]   G. A. Niklasson, in *Materials Science for Solar Energy Conversion Systems*, (Ed: C. G. Granqvist), Pergamon Press, Oxford, UK **1991**, 7.

[15]   J. M. Garnett, *Philos. Trans Royal Soc. London. Series A* **1904**, *203*, 385.

[16]   A. Earp, G. Smith, *J. Phys. D: Appl. Phys.* **2011**, *44*, 255102; J. Schmelzer Jr, S. Brown, A. Wurl, M. Hyslop, R. Blaikie, *Phys. Rev. Lett.* **2002**, *88*, 226802.

[17]   M. Bilokur, A. R. Gentle, M. D. Arnold, M. B. Cortie, G. B. Smith, *Solar Energy Mater. Solar Cells* **2019**, *200*, 109964.

[18]   S. B. Jones, S. P. Friedman, *Water Resources Research* **2000**, *36*, 2821.

[19]   O. D. Miller, C. W. Hsu, M. H. Reid, W. Qiu, B. G. DeLacy, J. D. Joannopoulos, M. Soljačić, S. G. Johnson, *Phys. Rev. Lett.* **2014**, *112*, 123903.

[20]   T. Tesfamichael, E. Wäckelgård, *Solar Energy* **2000**, *68*, 335.